J Nanopart Res (2011) 13:2147–2155
DOI 10.1007/s11051-010-9973-7

RESEARCH PAPER

Surface photovoltage properties and photocatalytic activities of nanocrystalline $CoFe_2O_4$ particles with porous superstructure fabricated by a modified chemical coprecipitation method

Zhengru Zhu · Xinyong Li · Qidong Zhao · Yong Shi · Hong Li · Guohua Chen

Received: 18 January 2010 / Accepted: 24 May 2010 / Published online: 10 June 2010

Abstract In this study, nanocrystalline $CoFe_2O_4$ particles with porous timber-like superstructure were synthesized by a modified chemical co-precipitation route with calcination temperatures of 573, 673, 773, 873, and 973 K, respectively. The structural properties of the samples were systematically investigated by X-ray powder diffraction, scanning electronic microscopy, energy-dispersive X-ray spectra, UV–Vis diffuse reflectance spectroscopy, and Fourier transform infrared spectroscopy techniques. The photo-induced charge separation in the samples was demonstrated by surface photovoltage (SPV) measurement. The photocatalytic performances of the $CoFe_2O_4$ samples were comparatively studied by the degradation of 4-chlorophenol under Xe lamp irradiation. The results indicated that the sample calcined at 673 K exhibited the highest photocatalytic efficiency among the five samples.

Z. Zhu · X. Li (✉) · Q. Zhao · Y. Shi · H. Li
Key Laboratory of Industrial Ecology and Environmental Engineering and State Key Laboratory of Fine Chemical, School of Environmental Sciences and Technology, Dalian University of Technology, Dalian 116024, China
e-mail: xyli@dlut.edu.cn; xinyongli@hotmail.com

X. Li · G. Chen
Department of Chemical and Biomolecular Engineering, The Hong Kong University of Science & Technology, Clear Water Bay, Kowloon, Hong Kong

Keywords Chemical co-precipitation · Calcination · Specific surface area · 4-Chlorophenol · Photocatalytic degradation · Catalysts

Introduction

With the growing interests in the development of functional materials with unique micro- or nanostructures, their fabrication methods as well as their fascinating size- and morphology-dependent properties are investigated actively (Trindade et al. 2001; Ayyappan et al. 2009; Bao et al. 2009; Tong et al. 2009). While the materials are produced with characteristic dimensions on nanoscale, such as nanopores, nano domains or assembled units of nanosheets, nanowires, etc., they exhibit novel features in various physical and chemical properties that are never found with their bulk forms, which are brought about by the large surface-to-volume ratio, spatially confined charges and possible surface and quantum effects originating from the tiny structures (Yoffe 2002; Roduner 2006; Pileni 2007; Evans et al. 2008; Wang et al. 2008a, b). Besides, the surface structures of the nanoparticles, which are vital for their macroscopic properties, could be further modified by changing the synthetic conditions or additional post-treatment.

The cubic-spinel-structured cobalt ferrite ($CoFe_2O_4$) has been widely studied due to its high electromagnetic

performance (Grigorova et al. 1998), excellent chemical stability, mechanical hardness, and high cubic magnetocrystalline anisotropy. These properties make $CoFe_2O_4$ materials suitable for many practical applications such as audio/video tape and high-density digital recording disks, etc. (Pallai and Shah 1996; Skomski 2003). Some synthetic methods have been developed to prepare $CoFe_2O_4$ ferrites and pure powders, including sol–gel (Christoskova et al. 2001), micro-emulsion (Li et al. 2001; Li and Kutta 2003), citrate gel (Yan et al.1999), precipitation (Rajendran et al. 2001), polymer complex (Montemayor et al. 2005), hydrothermal process (Cabarias and Poliakoff 2001), precursor techniques (Randhawa 2000; Prasad and Gajbhiye 1998; Li et al. 2004; Liu et al. 2005a; Liu et al. 2005b), alkalide reduction (Mooney et al. 2004), sonochemical reactions (Shafi et al. 1998), host template (Pham-Huu et al. 2003; Kommareddi et al. 1996), combustion method (Yan et al. 1999), and mechanical alloying (Shi et al. 2000; Manova et al. 2004). Among these methods, the chemical co-precipitation method is more favorable for its simplicity and good control of crystallite size in synthesizing magnetic oxides with nanostructures. Wang et al. (2008a, b) have reported on the preparation of nanocrystalline $ZnFe_2O_4$ by thermal decomposition of ferrioxalate precursor, which exhibited super-paramagnetic properties at room temperature. The method could be also extended to synthesize $CoFe_2O_4$ nanocrystals. Nevertheless, other versatile properties of nanocrystalline $CoFe_2O_4$ with timber-like superstructure, such as photoelectric, photocatalytic, and magnetoelectric functions, etc., still need further comprehensive exploration for practical applications.

In this article, nanocrystalline $CoFe_2O_4$ particles with porous timber-like superstructure were prepared by a modified chemical co-precipitation method along with post-calcinations at 573, 673, 773, 873, and 973 K to vary their crystallinity as well as their surface states. Their bulk and surface structures are systematically characterized. It is demonstrated that these porous timber-like $CoFe_2O_4$ nanostructures possess attractive photoelectric response in the visible region and remarkable photocatalytic activities in degradation of environmental pollutants. The performance decline for the samples calcinated at higher temperatures is also elucidated in terms of the surface structures and crystallite sizes.

Materials and methods

Materials and regents

The starting materials such as ferrous sulfate ($FeSO_4 \cdot 7H_2O$), cobalt sulfate ($CoSO_4 \cdot 7H_2O$), and sodium oxalate ($Na_2C_2O_4$) were purchased from Aldrich Chemical Company. 4-Chlorophenol (purchased from the National Fine Chemical Laboratory of DLUT) was used as target compound for degradation. Other chemicals and solvents were of analytical grade from Aldrich Chemical Company. All the compounds were used as received without further purification.

Preparation of catalysts

$CoFe_2O_4$ nanocrystals with timber-like superstructure were synthesized by a modified chemical co-precipitation method. The starting materials were ferrous sulfate ($FeSO_4 \cdot 7H_2O$) and cobalt sulfate ($CoSO_4 \cdot 7H_2O$). Sodium oxalate ($Na_2C_2O_4$) was used as the precipitation materials. Stoichiometric amounts of 0.1 M (100 mL) solution of $FeSO_4 \cdot 7H_2O$ and 0.2 M (100 mL) $CoSO_4 \cdot 7H_2O$ were mixed in deionized water. 0.3 M (25 mL) solution of sodium oxalate was prepared and added to the salt solution. The solution was kept at 353 K and allowed to cool slowly under continuous stirring. Certain amount of oleic acid was added to the solution as a surfactant. A yellowish cobalt ferrioxalate precipitate began to appear. The precipitate was then washed twice with distilled water and then with ethanol to remove the excess surfactant from the solution. To isolate the supernatant liquid, the beaker content was centrifuged for 15 min at 9000 rpm. The separated precipitate was then dried overnight at 373 K. The precursor was ground into a fine powder, which was divided into five portions and heated at 573, 673, 773, 873, and 973 K for 2 h, respectively, to yield five $CoFe_2O_4$ samples (labeled as S1, S2, S3, S4, and S5, respectively).

Characterizations of catalysts

The phase compositions and structures of the $CoFe_2O_4$ samples were determined by X-ray diffraction (XRD, RIGAKU, Dmax22000) with Cu Kα radiation ($\lambda = 0.15418$ nm) over the 2θ range of

25–80°. Light absorption properties were obtained using a UV–Vis diffuse reflectance spectrophotometer (JASCO, UV-550). The morphology of $CoFe_2O_4$ samples was observed by scanning electronic microscopy (SEM) with a JSM-6700 LV electron microscope operating at 5.0 kV, and the compositions were examined by energy-dispersive spectroscopy (EDS) in the SEM.

The nitrogen adsorption–desorption isotherms were measured at 77 K on a SA3100 surface area and pore size analyzer. Samples were degassed in a vacuum at 200 °C for 3 h prior to each measurement. The Brunauer–Emmett–Teller (BET) method was utilized to calculate the specific surface areas S_{BET}.

The chemical structures of $CoFe_2O_4$ samples were characterized by a Fourier transform infrared spectrophotometer (BRUKER VERTEX 70 Optics). Without additional pretreatment, the $CoFe_2O_4$ powder was sampled and pressed into pellets for test after mixed with KBr.

Photovoltaic measurements

Surface photovoltage (SPV) measurements were carried out on a lock in-based system, which consists of a xeon lamp (500 W), a sample cell, a computer-controlled monochromator (model Omni-λ3005) and a lock-in amplifier (model SR830-DSP) with an optical chopper (model SR540) running at 20 Hz. The AC photovoltage signal from the sample was detected using a sandwich-like structure of ITO/sample/ITO. The effective overlapping area of the two electrodes tested here is about 1 cm^2 for all the samples. The phase spectra were recorded on a computer synchronously with the SPV spectra. Calibration of the system was done to eliminate any ultra-phase shift that is not correlated to SPV response (Donchev et al. 2006), so that any phase-retardation detected is only correlated to the phase of the modulated light intensity and reflects the kinetics of developing SPV response. All the SPV measurements were operated under ambient conditions and at room temperature. The raw data were not treated further.

Measurements of photocatalytic activities

The photocatalytic oxidation of 4-chlorophenol was carried out in a single photochemical reaction system shown in Fig. 1. The initial concentration of the 4-CP

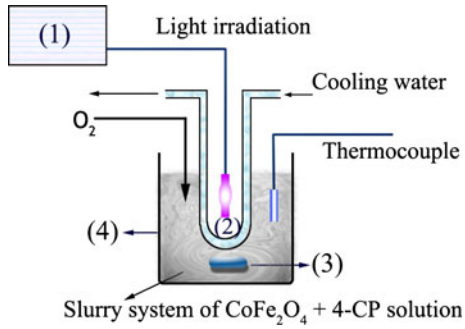

Fig. 1 Schematic of the photochemical reaction testing system. (*1*) Power controller, (*2*) light source of xenon lamp, (*3*) magnetic stirrer, (*4*) quartz photocatalytic reactor

aqueous solution was 20 mg L^{-1} during the experiment. An XQ-500W xenon lamp was used as the light source. All the experiments were performed with magnetic stirring. 0.01 g of the as-prepared $CoFe_2O_4$ powder was added into a quartz reactor containing 100 mL of 4-CP (C_6H_4ClO, 20 mg L^{-1}) solution. Before illumination, the suspension was magnetically stirred in the dark for 30 min to ensure adsorption equilibrium of 4-CP with the catalyst. After that it was exposed to xenon lamp irradiation. During the process of successive irradiation with stirring, 1 mL of the solution was withdrawn periodically for UV analysis.

Results and discussions

The crystalline phase of the $CoFe_2O_4$ samples

The crystallinities and phase purities of the as-prepared precursor and the calcined products were examined by powder X-ray diffraction (XRD). Figure 2a shows the XRD patterns of the precursor and the samples (S1, S2, S3, S4, and S5) after calcination at different temperatures. The results show that the final product is $CoFe_2O_4$ with the expected inverse spinel structure. The characteristic peaks of $CoFe_2O_4$ appearing at 30.7° (with index number of 220), 36.3° (311), 43.6° (400), 57.9° (511), and 63.2° (440) reveal the formation of $CoFe_2O_4$. No other phase was detected. From the broadened XRD peaks of the (311) using the Scherrer equation $D = 0.89\lambda/\beta\cos\theta$, the average sizes of these five samples are about 8 nm (S1), 12 nm (S2), 14 nm (S3), 16 nm (S4), and 21 nm (S5). The peak intensity enhances with increasing calcination temperature,

which indicates that the calcination temperature plays a role in the formation of spinel crystal structure and controlling the crystallite size. Using the Bragg law (Caizer and Stefanescu 2002), for any cubic system the relation between angle of diffraction and the lattice parameter is:

$$\sin^2\theta = \lambda^2\left(h^2 + k^2 + l^2\right)/4a^2 \quad (1)$$

where θ is the maximum peak position, λ is the incident cupper k_α wavelength of 1.5418 Å (h, k, l) are the Miller planes and a is the lattice parameter. The value of $\sin^2\theta$ and $h^2 + k^2 + l^2$ for the $CoFe_2O_4$ at different calcination temperatures is plotted in Fig. 2b, which shows a linear relationship between the $\sin^2\theta$ and the $h^2 + k^2 + l^2$ values. The lattice parameter is calculated from the slope of the curve. The measured values of lattice constant for the samples at different calcination temperatures are about 8.25 Å (S1), 8.23 Å (S2), 8.20 Å (S3), 8.19 Å (S4), and 8.19 Å (S5), which have a little difference compared to the reported value of 8.39 Å (JCPDS card no. 22-1086). This contrast on lattice parameter might be due to very high surface energy for the small-sized particles. Especially for samples calcined at higher temperature, the diffracted angle is shifted towards higher angle, which should be attributed to the decrease in the lattice parameter (Sun et al. 2004).

The morphology and the specific surface area of the $CoFe_2O_4$ samples

The SEM images in Fig. 3 show the morphology of the $CoFe_2O_4$ samples S1, S2, S3, S4, and S5. The calcined $CoFe_2O_4$ powders at different temperatures are all composed of timber-like small rods. The apparent particle dimensions of the samples are up to tens of micrometers. The SEM image in Fig. 3a (sample S1) shows that the surface of the "timbers" is very smooth, which is different from the other samples. The SEM images in Fig. 3b–f and the representative high-magnification SEM images in Fig. 3g further indicate that the blocks are of porous structures. It was found that the porous blocks were formed through the agglomeration of numerous nanocrystalline $CoFe_2O_4$ particles.

The successful preparation of $CoFe_2O_4$ samples is further demonstrated by the elemental signature in the EDS spectrum (Fig. 3h). The EDS spectrum exhibits Co, Fe, and O peaks and also reflects the atomic ratio of Co, Fe, and O in the prepared sample.

The BET specific surface areas of the $CoFe_2O_4$ samples at the calcination temperatures of 573, 673, 773, 873, and 973 K, are 8.261, 78.96, 26.360, 24.153, and 16.871 m^3g^{-1}. The sample S2 has larger specific surface area than the others, which enables it with larger surface area for adsorption of foreign species and will lead to higher photocatalytic degradation efficiency. The lowest BET specific surface area for the sample S1 could be attributed to the low temperature of calcination, which did not decompose the precursor sufficiently to form the porous blocks.

The chemical structures of the $CoFe_2O_4$ samples

Figure 4 shows the FT-IR spectra of S1, S2, S3, S4, and S5, respectively. The typical metal-oxide vibration band characteristic of $CoFe_2O_4$ (543–594 cm^{-1}) correlated with the spinel structure characteristics of $CoFe_2O_4$ is observed in the FTIR spectra for all the

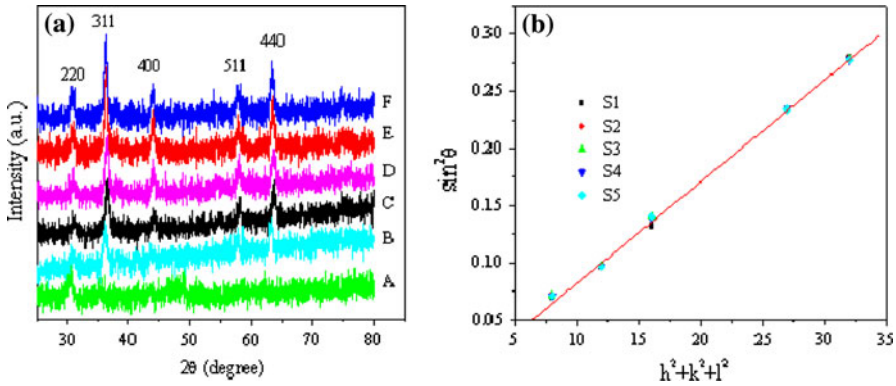

Fig. 2 **a** XRD patterns of as-prepared precursor (*A*) and the calcined $CoFe_2O_4$ samples S1 (*B*), S2 (*C*), S3 (*D*) S4 (*E*), and S5 (*F*). **b** The linear dependence of $\sin^2\theta$ versus $h^2 + k^2 + l^2$ of the $CoFe_2O_4$ samples synthesized under calcination temperatures of 573, 673, 773, 873, and 973 K, respectively. The best fit is shown by *solid line*

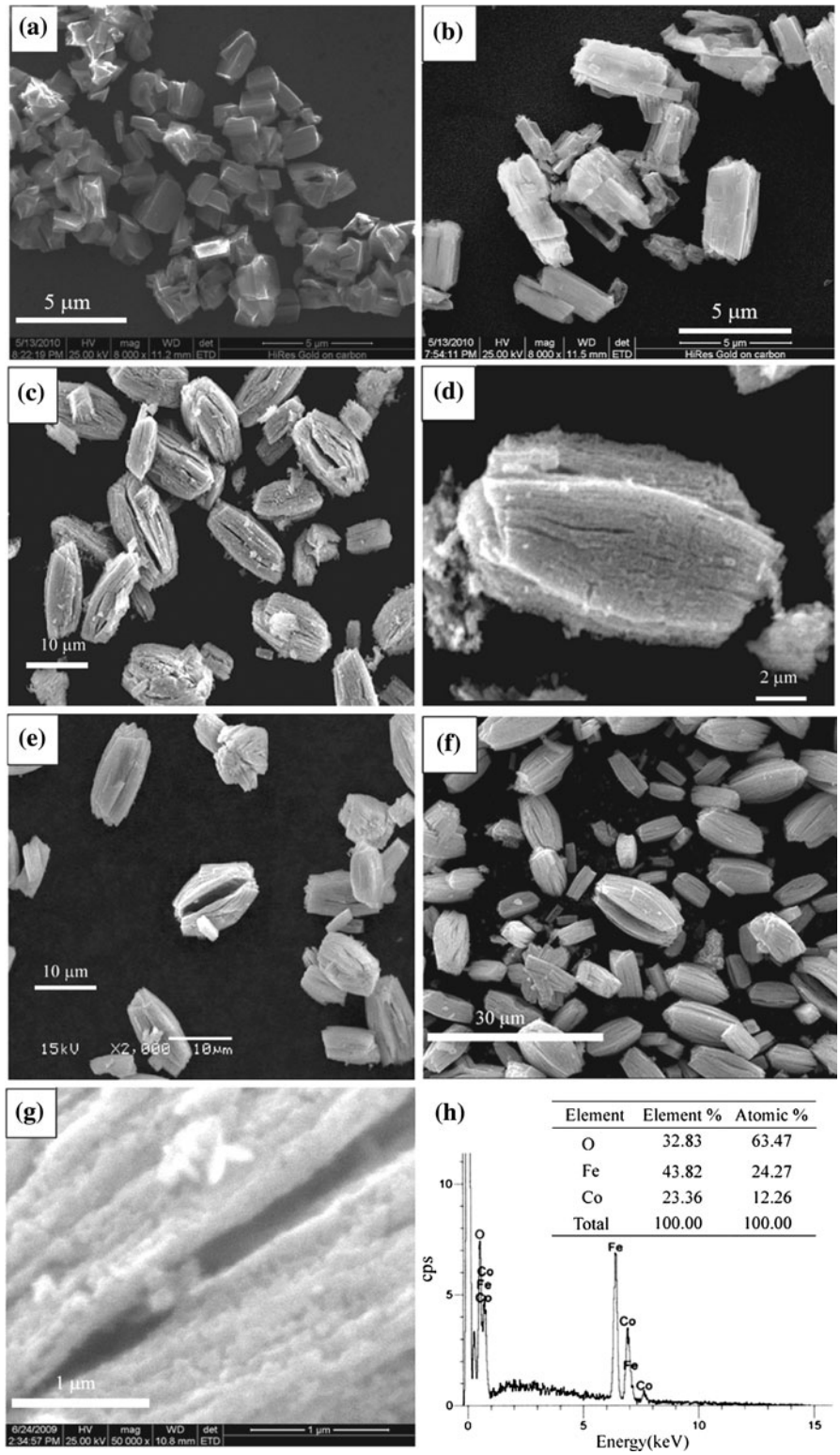

Fig. 3 SEM images of S1 (**a**), S2 (**b**), S3 (**c**, **d**, **g**), S4 (**e**), and S5 (**f**). **h** EDS pattern of S3

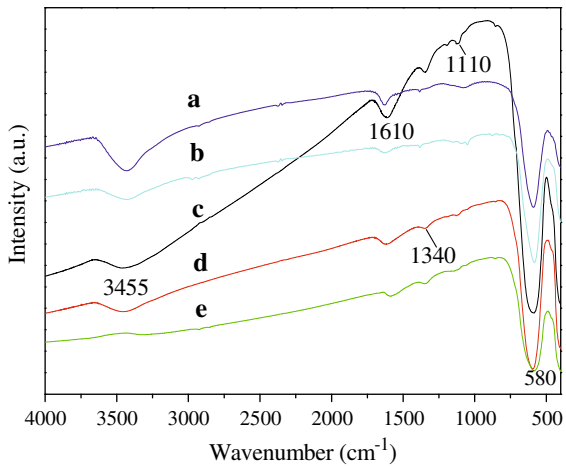

Fig. 4 Infrared absorption spectra of S1 (*a*), S2 (*b*), S3 (*c*), S4 (*d*), and S5 (*e*)

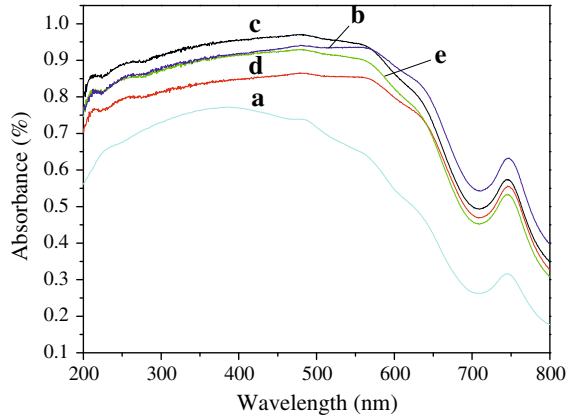

Fig. 5 UV–Vis absorption spectra of S1 (*a*), S2 (*b*), S3 (*c*), S4 (*d*), and S5 (*e*)

calcined samples. The band at 580 cm^{-1} strongly suggests the intrinsic stretching vibrations of the Fe–O bond at the tetrahedral site (Selvan et al. 2008; Randhawa 2000). The intensive broad band at 3432–3455 cm^{-1} and the less intensive band at 1610–1655 cm^{-1} are due to O–H stretching vibration interacting through H bonds (Sangmanee and Maensiri 2009). The peak appears at 1345 cm^{-1}, which is characteristic of C–O–O symmetric stretch (Limaye et al. 2009).The band at 1110 cm^{-1} are associated with the C–O–C symmetrical stretching vibration (Liu et al. 2009). For all the samples, the adsorbed water molecules (i.e., O–H bond) (Limaye et al. 2009) become weaken and even vanish as the annealing temperature increases.

UV–Vis DRS analysis of the $CoFe_2O_4$ samples

The UV–Vis absorption spectra of the $CoFe_2O_4$ samples S1, S2, S3, S4, and S5 are shown in Fig. 5. In the whole visible light region, the absorption intensity of S2 and S3 is increased, which reveals that S2 and S3 are more sensitive to the visible light than the other samples. Therefore, a better photocatalytic capability for S2 and S3 under visible light is expected.

Surface photovoltaic analysis of the $CoFe_2O_4$ samples

The SPV method is a well-established noncontact technique for the characterization of semiconductors, which relies on analyzing illumination-induced changes in the surface voltage (Kronik and Sapira 1999; Zhai et al. 2000). The obtained SPV amplitude and phase spectra for these five samples are presented in Fig. 6a. The sample S2 exhibits distinguished SPV response, and its performance is evidently higher than those of the other samples. Unlike the UV–Vis spectra, which covers all types of photon absorption, the SPV spectra are only sensitive to the electron transition-related process and subsequent charges separation. The higher SPV signal may suggest the higher separation rate of photo-generated charge carriers (Liu et al. 2007). As shown in Fig. 6b, the normalized SPV spectra, S1, S3, and S4 have a similar SPV onset at about 520 nm with tail extending to 600 nm, whereas S2 and S5 both have a red shift of 50 nm with respected to the other three-ones.

The corresponding SPV phase values for S1, S2, S3, and S4 at wavelengths below 500 nm are around 90° (Fig. 6a, inset) smaller than 180°, which implies that the photo-generated electrons are accumulated to the surface of sample upon excitation (Donchev et al. 2006). According to the phase value and the physical state of powder layer, the diffusion-controlled charge separation dynamics dominates, which means that charge separation and surface charge accumulation in the sample do not reach equilibrium but increasing with time in an illuminating period under the chopped light modulation. It could be observed by comparison that S2 has steady phase retardation on the whole spectrum, which could be attributed to its faster photo-induced charges transfer rate between grains

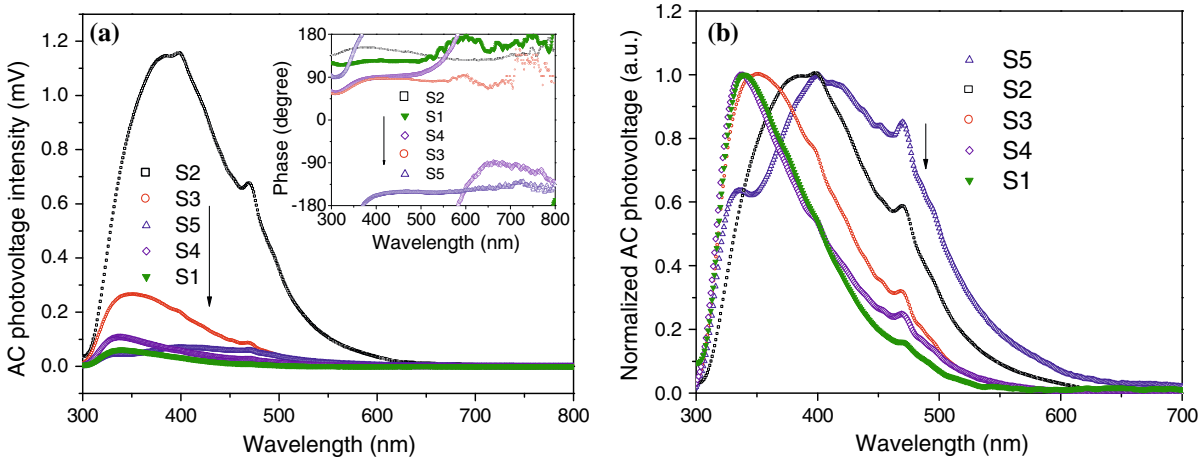

Fig. 6 **a** SPV spectra and corresponding phase spectra (*inset*) of S1, S2, S3, S4, and S5. **b** Normalized SPV spectra of S1, S2, S3, S4, and S5

upon illumination as well as the increased rate of charge recombination in the dark.

Due to the quantum confinement effect, the electronic band gaps of the dispersed nanocrystals in the "timber-like" aggregation of S1, S2, and S3 are widened with respect to S4 and S5, which would improve the redox activity of their photo-generated electrons and holes correspondingly. However, for comparison among the samples on the SPV intensity, the SPV response by S2 is significantly larger than the others, and the SPV response for S3 is much larger than S4 or S5. This difference implies the charge separation efficiency is the highest for S2, so that the best photocatalytic activity could be expected for S2.

The photocatalytic properties of the $CoFe_2O_4$ samples

The photocatalytic activities of the $CoFe_2O_4$ samples were evaluated by the photocatalytic degradation of 4-CP solution under xenon lamp irradiation. As can be clearly seen in Fig. 7, the 4-CP in aqueous solution can be hardly degraded without catalyst under illumination. After 120 min of irradiation, the 4-CP in aqueous solution can be degraded by these $CoFe_2O_4$ samples, whereas the degradation ratios of S1, S2, S3, S4, and S5 are 47.2, 79.2, 70.1, 59.9, and 52.2%, respectively. This result illustrates that S2 has the highest photocatalytic activities among these samples. The linear correlation between ln (C_0/C_t) and t (C_0 is the initial concentration of 4-CP, C_t is the concentration of 4-CP at time t, and k is kinetic constant) suggests a pseudo-first-order reaction in all the processes. The corresponding kinetic constants and regression coefficients are given in Table 1. Under the same experimental conditions, the kinetic constant of 4-CP photocatalysis with S2 is 2.2 and 1.2 times as large as that of S1 and S5, respectively, and similar to those of S3 and S4.

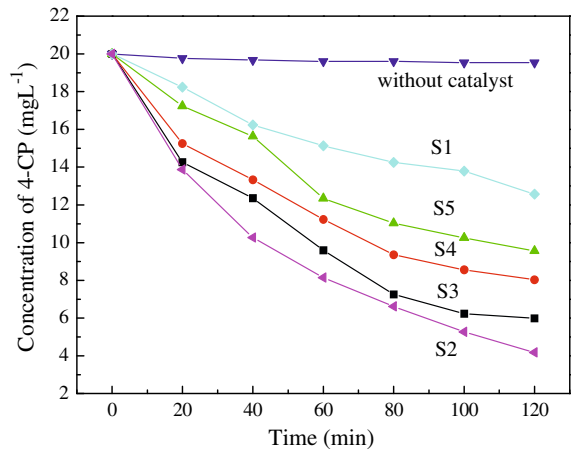

Fig. 7 The photocatalytic degradation of 4-CP with S1, S2, S3, S4, and S5 as well as its photolysis without any catalysts

According to the above results, S2 could have more objective substrates at its surface due to its higher specific surface area. Meanwhile, XRD study shows that the crystallite size of S1 is smaller than the others. With the decreasing of the crystallite size, the

Table 1 Kinetic constants and regression coefficients of photocatalytic degradation of 4-chlorophenol under xenon lamp irradiation ($I_0 = 71.4$ mW cm^{-2})

Processes	Kinetic constants (k, h^{-1})	R^2
Photocatalytic degradation without $CoFe_2O_4$ catalyst	0.00396	0.89777
Photocatalytic degradation with S1	0.02739	0.98811
Photocatalytic degradation with S2	0.06042	0.99494
Photocatalytic degradation with S3	0.08641	0.98484
Photocatalytic degradation with S4	0.06546	0.98378
Photocatalytic degradation with S5	0.05215	0.98563

band gap of $CoFe_2O_4$ nanocrystals should be widened, favoring the redox activity of the photo-induced charges. But this factor is not the crucial one determining its photocatalytic activity, as indicated by the photocatalysis results. The lowest BET specific surface area for the sample S1 should account for its poor activity.

The enhanced SPV response and higher photocatalytic activity of S2 reveal that the separation efficiency of photo-induced electron–hole pairs into charge carriers is much improved, contributing to the subsequent photocatalytic process significantly. The photo-generated holes with longer lifetime would have more opportunity to oxidize the substrate before re-combination with the electrons. Therefore, the porous $CoFe_2O_4$ with timber-like superstructure calcined at 673 K exhibits the higher photocatalytic activity than the other samples calcined at higher temperatures.

Conclusions

In summary, nanocrystalline $CoFe_2O_4$ particles with porous superstructure were prepared by a modified chemical co-precipitation method along with post-calcinations. These porous $CoFe_2O_4$ particles possess attractive photovoltage response in the visible region and remarkable photocatalytic activities in degradation of 4-CP. The porous timber-like superstructure is corresponding to the well spatial dispersion of the constituent nanocrystals, which ensures the adsorption capability and higher photo-induced reactivity. The performance decline for the samples calcinated at higher temperatures is due to the loss of specific surface area. The optimized performance in surface photovoltage response and photocatalytic degradation of environmental pollutants could be obtained for the sample with calcination at proper temperature, such as 673 K. The nanocrystalline $CoFe_2O_4$ particles with porous superstructure investigated here could be potentially applied in environmental purification and solar energy harvest in the near future.

Acknowledgments This work was supported financially by the National Nature Science Foundation of China (Nos. 20877013, 20837001), the National High Technology Research and Development Program of China (863 Program) (No. 2007AA061402) and the Major State Basic Research Development Program of China (973 Program) (No. 2007CB613306).

References

Ayyappan S, Philip J, Raj B (2009) Effect of digestion time on size and magnetic properties of spinel $CoFe_2O_4$ nanoparticles. J Phys Chem C 113:590–596

Bao N, Shen L, An W, Padhan P, Turner CH, Gupta A (2009) Formation mechanism and shape control of monodisperse magnetic $CoFe_2O_4$ nanocrystals. Chem Mater 21:3458–3468

Cabarias A, Poliakoff M (2001) The continuous hydrothermal synthesis of nano-particulate ferrites in near critical and supercritical water. J Mater Chem 11:1408–1416

Caizer C, Stefanescu M (2002) Magnetic characterization of nanocrystalline Ni–Zn ferrite powder prepared by the glyoxylate precursor method. J Phys D 35:3035–3042

Christoskova SG, Stoyanova M, Georgieva M (2001) Low-temperature iron-modified cobalt oxide system part I. Preparation and characterisation. Appl Catal A 208:235–242

Donchev V, Kirilov K, Ivanov Ts, Germanova K (2006) Surface photovoltage phase spectroscopy—a handy tool for characterisation of bulk semiconductors and nanostructures. Mat Sci Eng B 129:186–192

Evans G, Kozhevnikov IV, Kozhevnikova EF, Claridge JB, Vaidhyanathan R, Dickinson C, Wood CD, Cooper AI, Rosseinsky MJ (2008) Particle size–activity relationship for $CoFe_2O_4$ nanoparticle CO oxidation catalysts. J Mater Chem 18:5518–5523

Grigorova M, Blythe HJ, Blaskov V, Rusanov V, Petkov V, Masheva V, Nihtianova D, Martinez LM, Mun JS, Mikhov M (1998) Magnetic properties and Mossbauer

spectra of nanosized $CoFe_2O_4$ powders. J Magn Magn Mater 183:163–172

Kommareddi NS, Tata M, John VT, McPherson GL, Herman MF, Lee YS, O'Connor CJ, Akkara JA, Kaplan DL (1996) Synthesis of superparamagnetic polymer-ferrite composites using surfactant microstructures. Chem Mater 8:801–809

Kronik L, Sapira Y (1999) Surface photovoltage phenomena: theory, experiment, and applications. Surf Sci Rep 37: 1–206

Li X, Kutta C (2003) Synthesis and characterization of superparamagnetic $Co_xFe_{3-x}O_4$ nanoparticles. J Alloys Compd 349:264–268

Li S, Liu L, John VT, O'Connor CJ, Harris VG (2001) Cobalt–ferrite nanoparticles: correlations between synthesis procedures, structural characteristics and magnetic properties. IEEE Trans Magn 37:2350–2352

Li F, Liu JJ, Evans DG, Duan X (2004) Stoichiometric Synthesis of pure MFe_2O_4 (M = Mg, Co and Ni) spinel ferrites from tailored layered double hydroxide (hydrotalcite-like) precursors. Chem Mater 16:1597–1602

Limaye MV, Singh SB, Sadgopal KD, Kothari D, Reddy VR, Gupta A, Sathe V, Choudhary RJ, Kulkarni SK (2009) High coercivity of oleic acid capped $CoFe_2O_4$ nanoparticles at room temperature. J Phys Chem B 113:9070–9076

Liu XM, Fu SY, Huang CJ (2005a) Synthesis and magnetic characterization of novel $CoFe_2O_4$–$BiFeO_3$ nanocomposites. Mater Sci Eng B 121:255–260

Liu XM, Fu SY, Xiao HM (2005b) Synthesis of nanocrystalline spinel $CoFe_2O_4$ via a polymer-pyrolysis route. Physica B 370:14–21

Liu ZY, Sun DD, Guo P, Leckie JO (2007) An efficient bicomponent TiO_2/SnO_2 nanofiber photocatalyst fabricated by electrospinning with a side-by-side dual spinneret method. Nano Lett 7:1081–1085

Liu H, Xu F, Li LC, Wang YP, Qiu HZ (2009) A novel $CoFe_2O_4$/polyacrylate nanocomposite prepared via an in situ polymerization in emulsion system. React Funct Polym 69:43–47

Manova E, Kunev B, Paneva D, Mitov I, Petrov L, Estournès C, D'Orléans C, Rehspringer JL, Kurmoo M (2004) Mechano-synthesis, characterization, and magnetic properties of nanoparticles of Cobalt ferrite, $CoFe_2O_4$. Chem Mater 16:5689–5696

Montemayor SM, Cerda LAG, Lubian JRT (2005) Structural evolution during crystallization of β-BaB_2O_4 thin films fabricated by chemical solution deposition technique. Mater Lett 59:1056–1061

Mooney KE, Nelson JA, Wagner MJ (2004) Superparamagnetic cobalt ferrite nanocrystals synthesized by alkalide reduction. Chem Mater 16:3155–3161

Pallai V, Shah DO (1996) Synthesis of high-coercivity cobalt ferrite particles using water-in-oil microemulsions. J Magn Magn Mater 163:243–248

Pham-Huu C, Keller N, Estournès C, Ehret G, Grenèche JM, Ledoux M (2003) Microstructural investigation and magnetic properties of $CoFe_2O_4$ nanowires synthesized inside carbon nanotubes. J Phys Chem Chem Phys 5:3716–3723

Pileni MP (2007) Control of the size and shape of inorganic nanocrystals at various scales from nano to macrodomains. J Phys Chem C 111:9019–9038

Prasad S, Gajbhiye NS (1998) Magnetic studies of nanosized nickel ferrite particles synthesized by the citrate precursor technique. J Alloy Compd 265:87–92

Rajendran M, Puller RC, Bhattacharya AK, Das D, Chintalapudi SN, Majumdar CK (2001) Magnetic properties of nanocrystalline $CoFe_2O_4$ powders prepared at room temperature: variation with crystallite size. J Magn Magn Mater 232:71–83

Randhawa BS (2000) Preparation of ferrites from the thermolysis of transition metal ferrioxalate precursors. J Mater Chem 10:2847–2852

Roduner E (2006) Size matters: why nanomaterials are different. Chem Soc Rev 35:583–592

Sangmanee M, Maensiri S (2009) Nanostructures and magnetic properties of cobalt ferrite ($CoFe_2O_4$) fabricated by electrospinning. Appl Phys A 97:167–177

Selvan RK, Krishnan V, Augustin CO, Bertagnolli H, Kim CS, Gedanken A (2008) Investigations on the structural, morphological, electrical, and magnetic properties of $CuFe_2O_4$–NiO nanocomposites. Chem Mater 20:429–439

Shafi KVPM, Gedanken A, Prozorov R, Balogh J (1998) Sonochemical preparation and size-dependent properties of nanostructured $CoFe_2O_4$ particles. Chem Mater 10: 3445–3450

Shi Y, Ding J, Yin H (2000) $CoFe_2O_4$ nanoparticles prepared by the mechanochemical method. J Alloys Compd 308: 290–295

Skomski R (2003) Nanomagnetics. J Phys Condens Mater 15:R841–R896

Sun S, Zeng H, Robinson DB, Raoux S, Rice PM, Wang SX, Li G, Am J (2004) Monodisperse MFe_2O_4 (M Fe, Co, Mn) nanoparticles. Chem Soc 126:273–279

Tong J, Bo L, Li Z, Lei Z, Xia C (2009) Magnetic $CoFe_2O_4$ nanocrystal: a novel and efficient heterogeneous catalyst for aerobic oxidation of cyclohexane. J Mol Catal A 307:58–63

Trindade T, Brien PO, Pickett NL (2001) Nanocrystalline semiconductors: synthesis, properties, and perspectives. Chem Mater 13:3843–3858

Wang M, Ai Z, Zhang L (2008a) Generalized preparation of porous nanocrystalline $ZnFe_2O_4$ superstructures from zinc ferrioxalate precursor and its superparamagnetic property. J Phys Chem C 112:13163–13170

Wang Z, Liu X, Lv M, Chai P, Liu Y, Zhou X, Meng J (2008b) Preparation of one-dimensional $CoFe_2O_4$ nanostructures and their magnetic properties. J Phys Chem C 112:15171–15175

Yan CH, Xu ZG, Cheng FX, Wang ZM, Sun LD, Liao CS, Jia JT (1999) Nanophased $CoFe_2O_4$ prepared by combustion method. Solid State Commun 111:287–291

Yoffe AD (2002) Low-dimensional systems: quantum size effects and electronic properties of semiconductor microcrystallites (zero-dimensional systems) and some quasi-two-dimensional systems. Adv Phys 51:799–890

Zhai QZ, Qiu SL, Xiao FS, Zhang ZT, Shao CL, Han Y (2000) Preparation, characterization, and optical properties of the host-guest nanocomposite material zeolite-silver iodide. Mater Res Bull 35:59–73